

Finite Element Modeling of Optic Nerve Head Biomechanics

Ian A. Sigal,^{1,2} John G. Flanagan,^{3,4} Inka Tertinegg,³ and C. Ross Ethier^{1,2,3}

PURPOSE. Biomechanical factors have been implicated in the development of glaucomatous optic neuropathy, particularly at the level of the lamina cribrosa. The goal of this study was to characterize the biomechanics of the optic nerve head using computer modeling techniques.

METHODS. Several models of the optic nerve head tissues (pre- and postlaminal neural tissue, lamina cribrosa, central retinal vessel, sclera, and pia mater) were constructed. Stresses, deformations, and strains were computed using finite element modeling for a range of normal and elevated intraocular pressures. Computed retinal surface deformations were compared with measured deformation patterns in enucleated human eyes. A sensitivity analysis was performed in which tissue properties and selected geometric features were varied.

RESULTS. Acute IOP-induced deformation of the vitreoretinal interface was highly dependent on optic cup shape but showed a characteristic "W-shaped" profile that did not match the deformation of the anterior surface of the lamina cribrosa. The central retinal vasculature had surprisingly little effect on optic nerve head biomechanics. At an IOP of 50 mm Hg, strains (fractional elongation) in the lamina cribrosa averaged 4% to 5.5%, dependent on model geometry, with maximum strains up to 7.7%. Strains in the lamina cribrosa were more dependent on scleral stiffness, scleral thickness, and scleral canal diameter than on lamina cribrosa stiffness and optic cup shape.

CONCLUSIONS. Computed levels of strain in the lamina cribrosa are biologically significant and capable of contributing to the development of glaucomatous optic neuropathy, even without considering the probable accentuating effect of the lamina cribrosa's microarchitecture. Depending on optic cup shape, IOP-induced deformation of the vitreoretinal interface may not match lamina cribrosa deformation. This finding implies that scanning laser tomography has limited ability to estimate lamina cribrosa deformation when imaging the anterior topography of the optic nerve head. Biomechanical effects in the lamina cribrosa depend strongly on scleral properties. (*Invest Ophthalmol Vis Sci.* 2004;45:4378–4387) DOI:10.1167/iovs.04-0133

From the ¹Department of Mechanical and Industrial Engineering, the ²Institute for Biomaterials and Biomedical Engineering, and the ³Department of Ophthalmology and Vision Sciences, University of Toronto, Toronto, Ontario, Canada; and the ⁴School of Optometry, University of Waterloo, Waterloo, Ontario, Canada.

Presented in part at the annual meeting of the Association for Research in Vision and Ophthalmology, Fort Lauderdale, Florida, May 2003.

Supported by the Canadian Institutes of Health Research (CRE, JGF), Glaucoma Research Society of Canada (JGF), and Consejo Nacional de Ciencia y Tecnología de México (CONACYT; IAS).

Submitted for publication February 10, 2004; revised July 8, 2004; accepted August 5, 2004.

Disclosure: **I.A. Sigal**, None; **J.G. Flanagan**, None; **I. Tertinegg**, None; **C.R. Ethier**, None

The publication costs of this article were defrayed in part by page charge payment. This article must therefore be marked "advertisement" in accordance with 18 U.S.C. §1734 solely to indicate this fact.

Corresponding author: C. Ross Ethier, Department of Mechanical and Industrial Engineering, 5 King's College Road, University of Toronto, Toronto, Ontario M5S 3G8, Canada; ethier@mie.utoronto.ca.

Elevated intraocular pressure (IOP) is associated with the development of glaucomatous optic neuropathy. However, the pathogenesis of retinal ganglion cell damage in this disease remains unclear and controversial.¹ It has been proposed that ischemia and IOP-induced mechanical stresses within the lamina cribrosa (LC) play a role in glaucomatous axonal damage.² To evaluate the possible role of mechanical stresses in glaucomatous optic neuropathy, a characterization of the biomechanical environment within and around the optic nerve head (ONH) is needed.

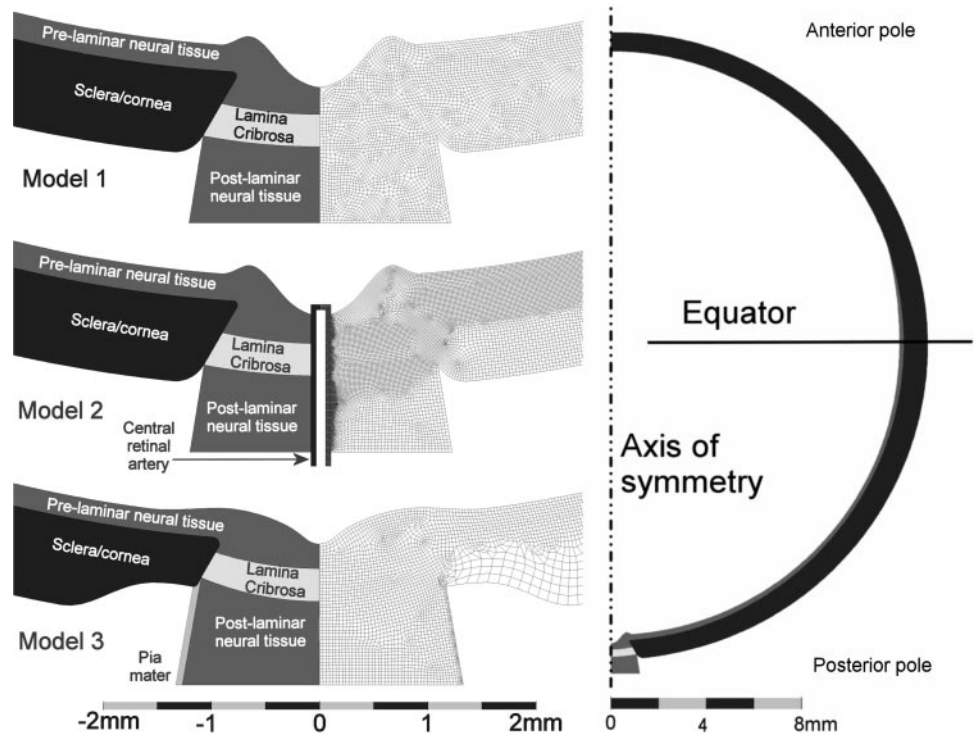
Several attempts have been made to measure ONH biomechanics experimentally. For example, the LC has been accessed directly to measure IOP-induced deformations by histologic³ and radiographic⁴ methods. Such measurements, although valuable, do not give a detailed picture of the biomechanical environment within the ONH. Scanning laser tomography allows measurement of the deformation of the vitreoretinal interface in real time, but provides little direct information about the biomechanics of the underlying sclera and LC. It therefore seems that the most fruitful approach to understanding LC biomechanics is a combination of experimental measurements and modeling studies.

Recently Dongqi and Zeqin⁵ and Edwards and Good⁶ developed analytical models of LC biomechanics. These models are valuable but are limited by the complex geometry of the ONH that forced the investigators to make simplifying assumptions. For instance, they assumed a perfectly circular LC of constant thickness and uniform elastic properties. Both assumptions are reasonable in the context of an analytic model, but limit the applicability of the results.⁷ The models also assume that a uniform pressure is applied to the anterior LC surface. Although the vitreous humor exerts a uniform pressure on the vitreoretinal interface, its action is not directly on the LC anterior surface. The forces on the anterior surface of the LC can be different from the pressure on the retinal surface and can even have a tangential component.

Computational models have been able to overcome some of the limitations described earlier. Bellezza et al.⁸ used finite element modeling to consider more complex geometries and material properties. They evaluated the effect of LC geometry, mainly eccentricity, on the stress distribution within the load-bearing tissues of the ONH. Although more comprehensive than previous analytical models, these computational models still rely on some critical assumptions—namely, constant LC thickness and a uniform IOP acting directly on the anterior LC surface.

In this work, we also used finite element modeling to quantify IOP-induced stresses and strains within the ONH. However, our models expand on previous work by considering the cross section of the ONH in greater detail and allowing for imposition of more realistic boundary conditions on the LC. Our goal was to investigate the effects of peripapillary sclera and prelaminar and postlaminal neural tissue on the overall biomechanical environment within the ONH. To do so, we introduced three simplified models of the ONH and computed stresses and strains acting on ONH tissues. We also performed a preliminary geometric sensitivity analysis and a parametric study of the effects of material properties.

FIGURE 1. Model geometries and meshes. Geometries for models 1, 2, and 3. *Left:* details of the ONH region and a typical finite element mesh formed by eight-node quadrilaterals. Note the small elements required in the blood vessel and the pia mater. Model 2 is a variation of model 1, with a central retinal vessel, and model 3 incorporates a slightly different geometry and the pia mater (see text for details). Scleral canal minimum diameter is 1.52 mm in models 1 and 2 and 1.83 mm in model 3. Anterior lamina surface diameter is 1.80 mm in models 1 and 2, and 1.90 mm in model 3. *Right:* full view of model 1, with axis of symmetry (dot-dashed line) and equator (solid line). All models have axial symmetry and, away from the ONH, are identical. Nodes on the equator and on the axis of symmetry are constrained to deform radially.



METHODS

The finite element method we used has found wide application in biomechanics, due to its ability to handle complex geometries.⁸⁻¹¹ It requires specification of the geometry of the modeled structure, the loads (forces) and constraints applied to that structure, and the elastic properties of the components. The geometry is subdivided into small regions (elements) and the differential equations governing the deformation of solids are numerically solved on the domain. Computed quantities include local deformations in response to the applied loads, as well as the corresponding stresses and strains. Strain is the fractional elongation of a solid element and is a generalization of the intuitive concept of stretch. Stress is the force acting within the material per cross-sectional area.

Geometry

Initially, three models were constructed, in increasing order of realism and complexity. Then variations of model 3 were constructed by independently varying scleral thickness, scleral canal diameter, and optic cup shape. All models were axisymmetric.

Model 1. Away from the ONH region the sclera-cornea formed a 0.78-mm thick spherical shell with a 12-mm internal radius.¹² In the ONH region, the sclera incorporated a scleral canal, tapered so as to have a diameter of 1.52 mm at the anterior opening. The prelaminar neural tissue included an optic cup and peripapillary rim in the ONH region. Farther from the ONH, the retina had a constant thickness of 0.24 mm before finally tapering away to zero thickness at 120° anterior of the axis of symmetry. The LC was modeled as a section of a spherical shell, concentric to the scleral-corneal shell, 0.3 mm thick with a 12.4 mm internal radius. The anterior and posterior faces of the LC had diameters of 1.80 and 2.14 mm, respectively (corresponding to an anterior LC surface area of 2.55 mm² vs. a measured value of 2.88 ± 0.72 mm²).¹³ The postlaminar optic nerve extended posteriorly from the LC and filled most of the scleral canal (Fig. 1).

Model 2. It has been suggested that the central retinal vessels have a mechanical effect on the deformation of the central region of the optic disc, acting like a tent pole.¹⁴ We therefore modified model 1 to include a simplified axisymmetric central retinal artery (CRA) with an external diameter of 0.18 mm and wall thickness of 0.05 mm, based

on approximate measurements of histologic sections through the center of the CRA (Fig. 1). The artery wall was assumed to be mechanically attached to the neural tissue of the ONH and to the LC, forcing them to deform together, whereas the anterior termination of the CRA was modeled as rigid so that it followed the local displacement of the vitreoretinal interface, approximating the *in vivo* situation in which the three-dimensional vascular tree moves with the retinal surface and in tandem with the LC.¹⁵

Model 3. We extended model 1 to include more physiologically faithful details. The shape and dimensions of model 3 were based on data from literature, as well as our own estimations from histologic sections. The model did not include blood vessels but considered both the pia mater and the thinning of the sclera-cornea near the ONH region (Fig. 1). The cup was shaped so that the cup-to-disc ratio was 0.3 when measured with respect to a level 0.05 mm below the retina surface at the rim. The LC was modeled to be 0.3 mm thick at the axis of symmetry and 0.27 mm at its periphery, with anterior and posterior diameters of 1.90 and 2.15 mm, respectively (corresponding to an anterior LC surface area of 2.83 mm²), within the ranges reported for human LC.^{13,16-18} Scleral canal diameter was 1.83 mm, again within the ranges reported in humans.^{19,20} We measured the pia mater and scleral thickness from sagittal histologic sections of the ONH region of human eyes fixed at an IOP of 15 mm Hg. Sections were selected to lie approximately centrally in the scleral canal, stained with picrosirius red to visualize connective tissue better, photographed, and measured with image-analysis software (Amira 3.0; TGS Inc., Bordeaux, France). We assigned the pia mater a thickness of 0.06 mm and the sclera a variable thickness, increasing from 0.46 mm at its thinnest point, adjacent to the canal, to 0.8 mm at 10° from the axis of symmetry.¹² The shortest distance between the anterior surface of the LC and cerebrospinal fluid space was 0.39 mm and between the anterior surface of the LC and the pia mater was 0.28 mm. The latter value is within the ranges reported by Jonas et al.¹⁸

Sensitivity Analysis on Model 3. Taking model 3 as the base geometry, we varied the scleral thickness away from the ONH from 0.6 to 1.0 mm,¹² while keeping ONH geometry within 15° of the axis of symmetry of the ONH unchanged. Canal diameter was varied from 1.3 to 2.2 mm, representing canal cross-sectional areas of 1.33 to 3.8 mm², within the ranges reported in human eyes.^{19,20} We constructed models

TABLE 1. Summary of Mechanical Properties of ONH Tissues

Tissue/Species	Author(s)	Young's Modulus (MPa)
Sclera		
Tree Shrew	Phillips and McBrien ²³	2.28
Tree Shrew	Siegrwart and Norton ²⁴	0.69–18.3
Bovine	Smolek ²⁵	3.8–9.0
Human	Woo et al. ²⁶	5.5
Human	Friberg and Lace ²⁷	1.8–2.9
Monkey	Downs et al. ²⁸	2.9–5.5
Porcine	Spörl E, et al. <i>IOVS</i> 2003;44:ARVO E-Abstract 3318	0.3
Human	Battaglioli and Kamm ²⁹	4.76
Human	Kobayashi et al. ³⁰	5.5
Neural tissue		
Porcine brain	Miller ³¹	0.03
Bovine brain	Guillaume et al. ³²	0.046
Monkey brain	Merz et al. ³³	0.010
Bovine retina	Jones et al. ³⁴	0.020
Cat spinal cord	Chang et al. ³⁵	0.2–0.6
Rabbit spinal cord	Ozawa et al. ³⁶	0.035
Lamina cribrosa		
Porcine	Spörl E, et al. <i>IOVS</i> 2003;44:ARVO E-Abstract 3318	0.1
Fit to human	Edwards and Good ⁶	0.14–0.38
Monkey	Bellezza et al. ³⁷	0.077–0.405
Pia mater		
Human	Zhivoderov et al. ³⁸	1.44–4.65
Human	Our computations based on measurements by Mazuchowski and Thibault ³⁹	2.5–65
Human	Brands ⁴⁰	1.86 (Shear modulus)

The Young's moduli chosen for this study were: sclera, 3 MPa; lamina cribrosa, 0.3 MPa; neural tissue, 0.03 MPa; pia mater, 3 MPa; and central retinal vessels, 0.3 MPa. Results of a parametric study based on these values are shown in Figure 7.

* As cited by Kleiven.⁴¹

with three different cup shapes, ranging from a steep to a gradual cup slope, but with identical internal ONH geometry, as shown in greater detail later.

Pressure Loads

A uniform IOP was applied to all interior surfaces of the eye—that is, the vitreoretinal interface and sclera-cornea anterior to the retinal termination. A range of IOPs from 0 to 50 mm Hg was considered. In model 2, constant arterial pressure of 55, 80, or 105 mm Hg was applied on the interior surface of the vessel wall. This represented a range of physiologic mean arterial pressures ($\frac{2}{3}$ diastolic + $\frac{1}{3}$ systolic), corrected for the hydrostatic difference between the eye and the brachial artery, and is consistent with measurements of the mean diastolic pressure in the ophthalmic artery of 51.8 mm Hg.^{21,22} External surfaces of the eye were subject to a pressure of 0 mm Hg (atmospheric pressure).

In addition to the IOP, the ONH is exposed to a hydrostatic pressure from the cerebrospinal fluid (CSF). We tested the effects of CSF pressures ranging from 0 to 15 mm Hg on each of the models (1, 2, and 3). Except when indicated, all data shown are for a CSF pressure of zero.

Material Properties

The mechanical properties of the tissues that constitute the ONH and surrounding structures are not completely known. For this initial study, all materials were assumed to be linearly elastic, isotropic, and incompressible, in which case all that was needed to characterize the tissue's biomechanical behavior was the modulus of elasticity (Young's modulus). Table 1 summarizes relevant moduli for the tissues under consideration, from which moduli of 3 and 0.03 MPa were chosen for sclera and neural tissue, respectively. The fact that neural tissue is two orders of magnitude more compliant than the sclera is consistent with the expectation that neural tissue is unlikely to bear significant load.

Mechanical modeling of the LC is complex. It is a composite of connective tissue with pores through which glial cells and nerve fibers pass. In this initial work we treated the LC as homogeneous, which implies that computed stresses and strains must be interpreted as mean values over an averaging region that is larger than several LC pores. It is expected that the LC should be stiffer than neural tissue but more compliant than sclera. Based on experimental tests with tissue strips, Spörl et al. estimated the Young's modulus for LC to be approximately 0.1 MPa, which is approximately three times less than the 0.3 MPa that they measured for sclera (Spörl E, et al. *IOVS* 2003;44:E-Abstract 3318). Bellezza³⁷ developed a model of the LC as a porous, oriented solid, and measured the orientation and solid fraction of the monkey LC. Our calculations, using their best-fit data for acute monkey LC deformation, give a range of Young's modulus from 0.077 to 0.405 MPa. It is clear that there is significant uncertainty about the stiffness of the LC. Based on all these considerations, we assigned a Young's modulus of 0.3 MPa to the LC.

We were unable to find measurements of the mechanical properties of the central retinal vessels in the literature, and hence we assigned the central retinal artery wall a Young's modulus of 0.3 MPa, equal to that of similar-sized vessels in other regions of the human body. There is little information about the Young's modulus of the pia mater. Kleiven⁴¹ reported an elasticity modulus between 1.44 and 4.65 MPa, citing Zhivoderov et al.,³⁸ whereas Brands⁴⁰ used 1.86 MPa for human meninges shear modulus. Mazuchowski and Thibault³⁹ measured the Young's modulus of the human spinal cord, with and without pia mater present. Assuming a pia mater thickness between 0.06 and 1.6 mm and a perfectly cylindrical sample 1 cm in diameter, we derived a pia mater modulus between 2.5 and 65 MPa. We assigned the pia mater a Young's modulus of 3 MPa, the same as for the sclera.

Parametric Study

The selection of specific mechanical properties for each of the tissues modeled required careful scrutiny. Not only could these properties

affect the results obtained from each model, but the inherent physiologic variability in mechanical properties could be important in ONH biomechanics. For better understanding of the effect of our choices, we solved model 3, varying the Young's modulus of each tissue independently over two orders of magnitude.

Numerical Details

Models were created, meshed, solved, and postprocessed using ANSYS 6.1 (Ansys, Inc., Canonsburg, PA). Finite element meshes were generated with nonuniform element density (Fig. 1). Two-dimensional, eight-node elements (Plane82 in Ansys) were used throughout. In preliminary studies, the effect of mesh refinement was investigated in a series of meshes with element counts ranging from 217 to 41,604, and various degrees of mesh size heterogeneity. The structural percentage error in energy norm (SEPC),⁴² a measure of the continuity of the stress field, was plotted as a function of mesh size, and results were considered to be mesh independent when the SEPC dropped below 3% in all regions. The results discussed in this work correspond to meshes with 6,556, 20,338, and 7,123 elements (46,023, 151,025, and 44,537 degrees of freedom) for models 1, 2, and 3 respectively. Model 2 required many more elements to guarantee accurate prediction of the deformations in and near the thin blood vessel wall. The geometry variation studies required remeshing the models, and care was taken to ensure that these were still sufficiently resolved by keeping element size and nodal density roughly constant.

Numerical solution of the governing equations is difficult for incompressible materials (Poisson ratio, $\nu = 1/2$), due to singular behavior. It is therefore common to use a value of ν close to, but not equal to $1/2$. Woo et al.⁴³ found that the use of this approximation had little effect on the results. We tested the effect of varying the Poisson ratio from 0.49 to 0.499999 and observed minor changes in the solution (e.g., $<0.15\%$ change in the average strain on the LC) and therefore used a value of $\nu = 0.49$ for all simulations.

Nodes on the equator were constrained to deform radially (Fig. 1), corresponding approximately to anterior-posterior restraint from the extraocular muscles. Nodes on the axis of symmetry were constrained to deform so that they remained on the symmetry axis. Solutions required <1 minute of CPU time on a desktop workstation (Windows XP SP1 [Microsoft Corp., Redmond, WA], and Athlon XP 2100+ CPU [AMD, Sunnyvale, CA] with 1 GB of memory).

Model Validation and Consistency Check

It is important to validate computational results; unfortunately, such validation is not trivial for the ONH. We compared acute IOP-induced deformations of the vitreoretinal interface as computed in our model with acute deformations measured in enucleated human eyes.

The experimental study used paired human eyes obtained within 24 hours after death from the Eye Bank of Canada, Ontario Division. Eyes were obtained and managed in accordance with the provisions of the Declaration of Helsinki for research involving human tissue. Eyes were required to have optic nerves at least 5 mm long and were excluded if there was a known history of disease expected to affect connective tissue mechanical properties (e.g., scleritis, rheumatoid arthritis) or a known history of high myopia (>8.0 D). The optic nerve was tied off at a distance of 3 mm from the posterior surface of the eye to prevent blood efflux. Eyes were surgically prepared using one of two experimental approaches that were improvements over our original technique.⁴⁴ In the first approach, two surgical infusion cannulae (MVS 1035; Storz Instrument Co., St. Louis, MO) were placed through the sclera and anterior pars plana 180° apart, thus allowing IOP control. The cornea was centrally trephined with an 8.5-mm trephine, and the iris and nucleus of the lens were removed. Capsular remnants and the core of the vitreous were then carefully removed with a vitrector (SITE-TXR; Site Microsurgical Systems Inc., Fort Washington, PA). The eye was rapidly refilled with isotonic saline and a specially designed optical apparatus was inserted into the hole trephined into the cornea. This device sealed against the margins of the cornea and incorporated a lens to replace the focusing power of the cornea and native lens. In

the second approach, we used eyes that had been used for corneal donation. The eye was opened circumferentially at the level of the pars plana, excising the anterior chamber, iris, and lens. The vitreous and lenticular remnants were removed by vitrectomy, as just described, and a modified apparatus, consisting of a collar incorporating two cannulae and a lens, was glued to the sclera with cyanoacrylate adhesive. This provided a fluid seal around the periphery of the incision while mechanically supporting the eye. Both approaches gave comparable results, although the collar system was somewhat easier to work with. This general technique had several important advantages: It protected the posterior half of the eye from mechanical stress; it replaced the possibly opaque cornea and lens in a postmortem eye with high-quality optics, permitting excellent quality images of the ONH; and it prevented retinal detachment.

The eye was gently wrapped with gauze soaked in isotonic saline and placed in a custom holder that was mounted to the vertical rails of a standard slit-lamp headrest. IOP was sequentially set to 5, 15, 22, 30, 40, and 50 mm Hg by adjusting the height of a reservoir containing isotonic saline. This reservoir was connected to one of the cannulas, and the other cannula was clamped off. Eye temperature was kept constant at 37° by a circulating water jacket attached to a constant-temperature bath. At each pressure, the eye was allowed to equilibrate for 15 minutes and incorporate viscoelastic effects into the deformation. Then, seven topographic image series (32 aligned scanning laser images, resolution = 256×256 pixels) were acquired with a 10° field of view centered on the nerve head using a scanning laser tomographer (Heidelberg Retinal Tomograph, ver. 2.01a; Heidelberg Engineering, Heidelberg, Germany). This protocol ensured good estimation of image variance⁴⁵ and stable ONH topography during imaging.³ The orientation of the eye was approximately determined by using insertion points of the extraocular muscles and was then adjusted by imaging and comparison of the relative locations of the macula and optic disc.

We computed the pressure-induced whole globe volume changes and compared them with the generalization of the Friedenwald ocular pressure-volume relation introduced by Silver and Geyer⁴⁶ as a consistency check. We also compared our model predictions of deformation with the topographic differences between average normal subjects and average patients with glaucoma developed by Swindale et al.,⁴⁷ using the HRT.

Analysis

Stresses and strains are tensors (i.e., dependent on orientation), and there is therefore no unique way to assign single values of strain and stress at a point. This makes graphical presentation of results difficult. Generally, values presented should have a reasonable physical or biological interpretation. In this work, we used the maximum principal strain and von Mises equivalent stress.⁴⁸ For an incompressible material, the maximum principal strains are nonnegative, always giving a measure of maximum extension. Von Mises equivalent stresses give an indication of the forces acting throughout the tissue, while discounting the effects of hydrostatic pressure. Because of assumptions used in this model, all stresses and strains scale linearly with the applied loads. Therefore, we report stresses as multiples of the imposed IOP.

Under the action of IOP the whole eye shell deforms. To observe only effects local to the ONH and allow for comparison with experiments, all computed anterior-posterior deformations were zeroed on the vitreoretinal interface at 5° from the center of the optic cup (the axis of symmetry), consistent with a 10° field-of-view HRT acquisition.

For each computed solution, the topography of the vitreoretinal interface at 15 mm Hg was subtracted from that at 50 mm Hg to provide a deformation map. For experimental measurements the deformation maps were obtained using the HRT's glaucoma progression analysis routines, which normalize for movement, rotation, tilt, and magnification changes. No zeroing was necessary for the computed difference between average normal and average glaucomatous topographies.

RESULTS

Figure 2 shows the undeformed shape of models 1, 2, and 3 at an IOP of 0 mm Hg (light lines) and deformed under an IOP of 50 mm Hg (dark lines), at true scale (left) and with the deformation exaggerated six times (right). Particularly evident is the “rotation” of the sclera as IOP increases, leading to appreciable stretching of the LC. Corresponding maps of computed vitreoretinal interface deformation as IOP increases from 15 to 50 mm Hg are shown in Figure 3. Also shown is an example of experimental results obtained from measurements taken on an enucleated human eye. Contour levels and colors are identical for all plots.

The deformation patterns can perhaps be better understood by plotting the computed deformation as a function of position away from the center of the optic cup, as in Figure 4. Each panel shows predictions for one model vitreoretinal and anterior LC surfaces. The wavy pink line corresponds to the experimental measurements shown in Figure 3, averaged circumferentially. Also shown in Figure 4 is a cross-section of the difference between average normal and average glaucomatous topographies of Swindale et al.⁴⁷ It can be seen that the LC displacement had a very different shape than the displacement of the vitreoretinal interface.

Under pressure, the prelaminar neural tissue and the LC displaced backward and thinned—for example, in model 1—as IOP increased from 15 to 50 mm Hg, on the axis of symmetry the thickness of the prelaminar and lamellar regions decreased by 10% and 8%, respectively. Prelaminar neural tissue was displaced laterally and posteriorly, so that the maximum deformation did not occur at the center of the cup. In contrast, maximum anterior LC deformation occurred at the center of

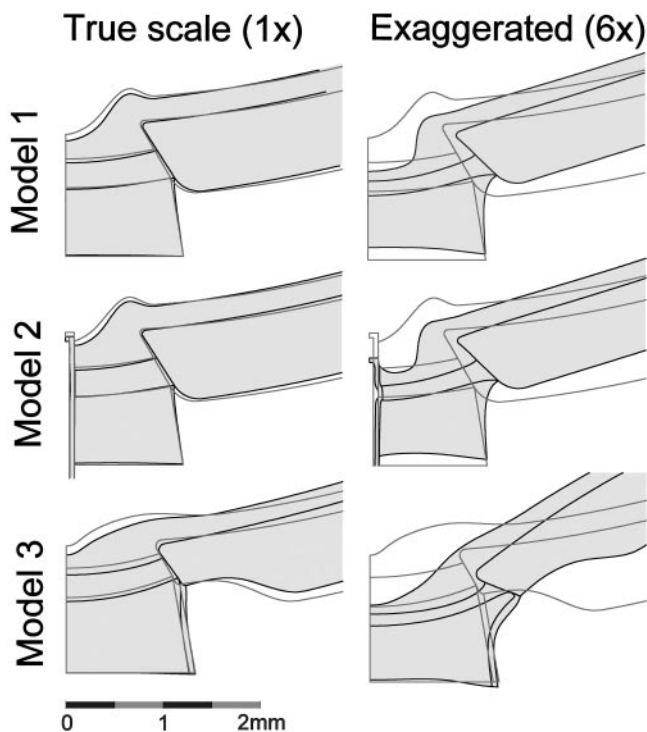


FIGURE 2. Deformations, true and exaggerated. Computed deformations for models 1, 2, and 3 as IOP increased from 0 mm Hg (light lines) to 50 mm Hg (heavy lines, shaded area). *Left:* true scale of the deformations; *right:* deformations exaggerated six times. All deformations were plotted so that the deformation of the vitreoretinal interface was zero at 5° from the center of the cup. Note the difference in “rotation” of the sclera between models 1 and 3. Results for model 2 are for a mean arterial pressure of 80 mm Hg.

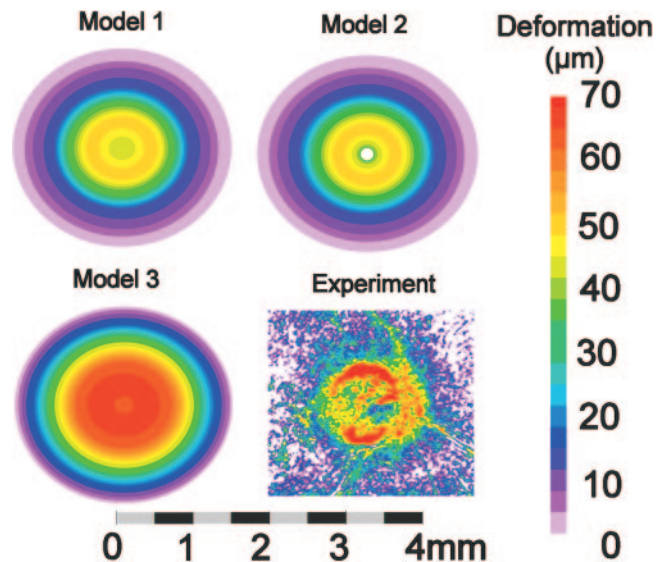


FIGURE 3. Computed deformation versus experiment. Comparison of computed vitreoretinal interface deformations with HRT-measured deformations (Experiment). The contoured quantity is the difference in topography of the vitreoretinal interface between IOPs of 15 and 50 mm Hg (see text for details on how the difference maps were computed). The experimental data were gathered from an eye of a 91-year-old male donor; histologic measurement showed a scleral canal minimum diameter of 1.60 mm and an anterior lamina surface diameter of approximately 1.90 mm (anterior LC area of 2.85 mm² vs. 2.55 mm² in model 1 and 2.84 mm² in model 3). Note that maximum displacement does not occur in the center of the optic cup.

the cup. The maximum LC deformation predicted for model 3 is approximately twice that of models 1 and 2.

Figure 5 shows computed distributions of maximum principal strain (left column) and von Mises equivalent stress (right column) for models 1, 2, and 3, under an IOP of 50 mm Hg. Table 2 presents a summary of these quantities in each region for each model. The largest stresses were observed in the relatively stiff sclera and pia mater, compared with the relatively soft neural and lamellar tissue. Incorporation of a simplified axisymmetric blood vessel, playing the role of the CRA, had surprisingly little effect on the strain and stress fields (top and middle rows).

In Figure 6 we show how maximum principal strain changes as the geometry of the model changes. Rows 1, 2, and 3 correspond to variations of model 3 with changes in scleral thickness, canal diameter, and cup shape, respectively. The undeformed configuration (IOP = 0 mm Hg) is shown with thick lines, and the deformed one (IOP = 50 mm Hg) is shown with the colored contour levels. Contour levels and colors are identical for all models. It can be seen, on the one hand, that changes in scleral thickness and scleral canal diameter had an appreciable effect on strains within the LC. On the other hand, changing cup shape had little effect on strains in the LC, although it affected deformation patterns in the prelaminar neural tissue.

Figure 7 shows average maximum principal strain within the LC as a function of Young's modulus. It can be seen that the strain within the LC depends critically on the stiffness of the sclera, being even more sensitive to scleral stiffness than LC stiffness.

In model 1, the internal volume of the entire globe increased by 60 and 175 μ L (0.8% and 2.3%) as IOP changed from 0 to 17 or 0 to 50 mm Hg, respectively. Using the ocular pressure-volume relation introduced by Silver and Geyer,⁴⁶ the corresponding volume changes for an eye with initial internal

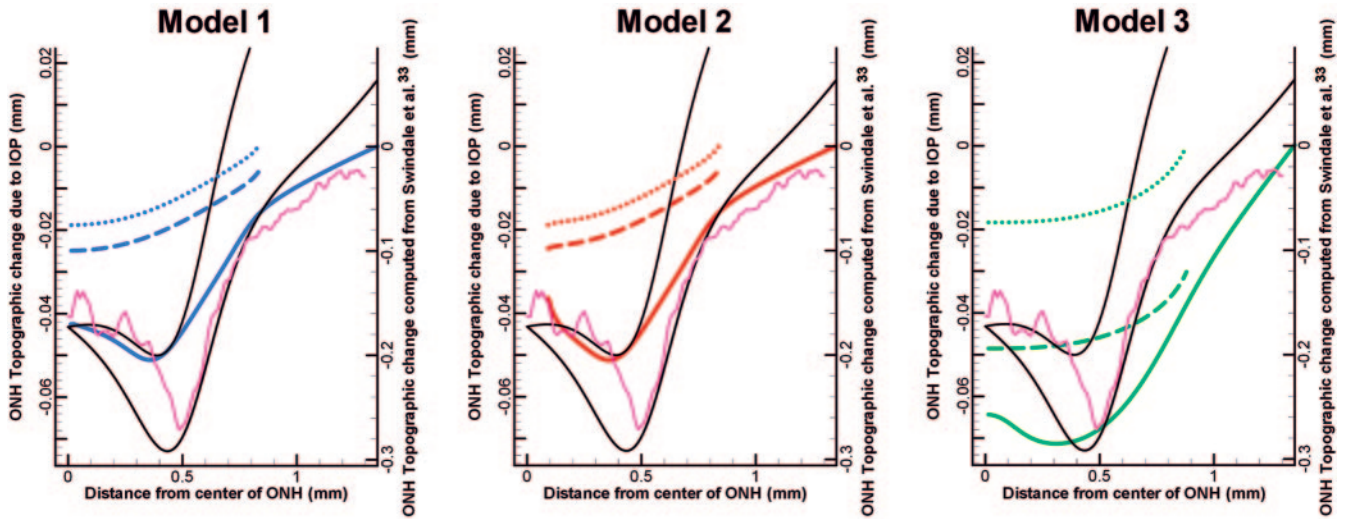


FIGURE 4. Computed deformation profiles. Plots of tissue displacement versus distance from center of the ONH as IOP increased from 15 to 50 mm Hg. *Solid lines:* vitreoretinal interface deformations; *broken lines:* LC anterior surface, either zeroed with the vitreoretinal interface (*dashed lines*) or at the LC edge (*dotted lines*). *Solid pink lines:* experimental measurements shown in Figure 2, circumferentially averaged (see text for details on how zeroing was applied). Also shown is a nasal-temporal cross section through the center of the optic disc of the difference between average normal and average glaucomatous topographies computed from the data of Swindale et al.⁴⁷ (*black lines* are to be read on right axis). There are two *black lines* because the displacement measured by Swindale et al. on the nasal side differs from that on the temporal side.

volume of 7680 μL were 50 and 100 μL (0.65% and 1.3%), respectively.

Increasing CSF pressure from 0 to 15 mm Hg at an IOP of 50 mm Hg changed the average maximum principal strain within the LC from 3.7% to 4.1% in model 1 and from 5.0% to 5.5% in model 3. These changes are small compared with the effects of geometry and material properties.

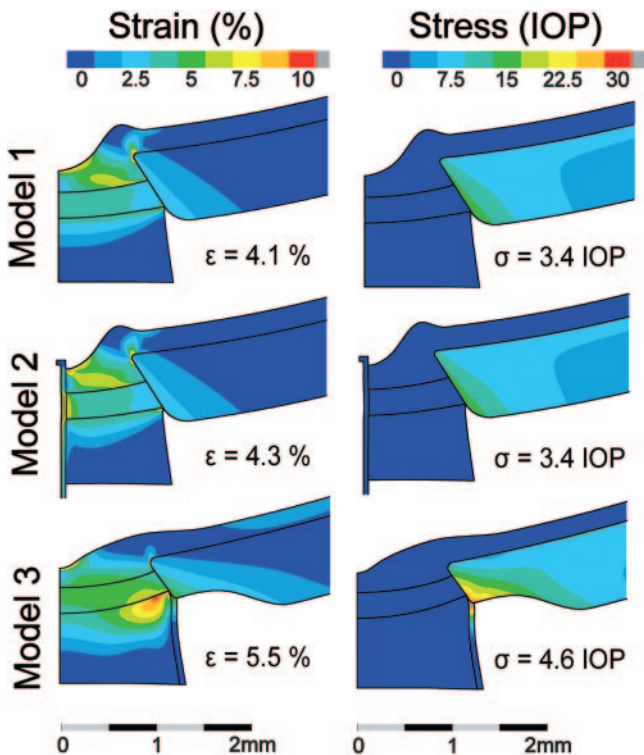


FIGURE 5. Strain and stress distributions. Contour plots of magnitude of computed distributions of maximum principal strain (*left*) and von Mises equivalent stress (*right*) in the ONH region in models 1, 2, and 3, at an IOP of 50 mm Hg. The geometry is shown at true deformation scale. Because of the nature of the models, the strain and stress scale linearly with pressure, and thus the stress is displayed as multiples of IOP. Maximum principal strain represents the magnitude of maximum extension. Von Mises equivalent stress gives an indication of the forces acting throughout the tissue, while discounting the effects of hydrostatic pressure. Below each computed result are the average maximum principal strain (ϵ) and von Mises equivalent stress (σ) within the LC.

DISCUSSION

The deformations of the vitreoretinal interface computed for models 1 and 2 were almost identical (Fig. 3, top and middle rows), but were quite different from that of model 3 (Fig. 3, bottom row), indicating that vitreoretinal deformation depends reasonably strongly on the assumed geometry of the ONH tissues. Both in the models and in the experiment, the maximum deformation occurred in a “ring” around the center of the cup.

The deformation profile of the anterior surface of the LC was slightly different between models 1, 2, and 3, but not remarkably so (Fig. 4). The main difference seemed to be in the slope at the edge, which was steeper in model 3, due to the “rotation” of the sclera (as seen in cross section), which causes the scleral angle of approach to the scleral canal to be larger in model 3 than in models 1 and 2 (Fig. 1 top vs. bottom). This difference in scleral displacement was probably due to a combination of two factors: a thinner peripapillary sclera and a larger scleral canal in model 3, as we can see from the sensitivity analysis (Fig. 6, top and bottom rows).

As expected, stiffening of any ONH component reduced strains in the LC, whereas softening had the opposite effect (Fig. 7). The weak dependence on pia mater modulus suggests that inclusion of the pia mater is probably not the source of the differences in strain magnitude and distribution between models 1 and 3.

Deformation of model 3 extended farther than the 5° used for zeroing and comparison with the HRT (Fig. 2, third row) and increased in thinner or more compliant scleral tissue (Fig. 6). This is consistent with a report by Heckell et al.,⁴⁹ who suggested that the peripapillary sclera could be deformed as far as 10° away from the center of the cup.

TABLE 2. Summary of Computed Maximum Principal Strains and von Mises Stresses for Each Tissue Region in Models 1, 2, and 3 at an IOP of 50 mm Hg

	Sclera/Cornea			Lamina Cribrosa			Prelaminar Neural Tissue			Postlaminar Neural Tissue			Blood Vessel Wall			Pia Mater		
	Model			Model			Model			Model			Model			Model		
	1	2	3	1	2	3	1	2	3	1	2	3	1	2	3	1	2	3
Average maximum principal strain (%)	1.5	1.5	1.9	4.1	4.3	5.5	1.8	1.7	2.1	1.5	2.4	3.2	*	4.4	*	*	*	1.6
Average von Mises stress (IOP)	9.3	9.6	12	3.4	3.4	4.6	0.17	0.17	0.17	0.12	0.19	0.23	*	2.2	*	*	*	9.8
Average of the highest 5% maximum principal strain (%)	3.0	3.1	4.1	5.0	7.7	6.4	6.8	6.6	5.8	4.6	4.7	7.4	*	10.7	*	*	*	5.7
Average of the highest 5% von Mises stress (IOP)	14	14	19	4.2	4.5	5.2	0.54	0.52	0.50	0.37	0.37	0.54	*	5.3	*	*	*	37

Only regions within 15° of the axis of symmetry on the posterior pole were considered for this table. The quoted highest values are computed as averages over the nodes having the largest 5% magnitudes, which largely eliminates the influence of outlier values (due, e.g., to mesh underresolution) and gives a fairer measure of the maximum stresses and strains.

* Tissue component was not present in a given model.

The agreement between IOP-induced increases in intraocular volume computed on our models with Silver and Geyer's formula⁴⁶ is good at physiologic pressures (60 vs. 50 μL), but less so at elevated pressures (175 vs. 100 μL), although within the range of normal values, probably because our model does not include the stiffening of tissue known to occur at higher elongations.

Through the variations in geometry shown in Figure 6, we see that the locations of strain concentration were independent of changes in scleral thickness, canal diameter, and cup shape. However, geometric changes, particularly scleral thickness and canal size, affected average maximum principal strain and von Mises equivalent stress in the LC. This supports the hypothesis that scleral thickness and disc size could be determinants for susceptibility to elevated IOP.^{8,50}

The effects of CSF pressure are complex, yet average maximum principal strain within the lamina is relatively unaffected by CSF pressures up to 15 mm Hg (<0.5% increase).

Main Conclusions

Four main conclusions arise from this work. First, the deformation of the vitreoretinal interface does not necessarily correspond to the deformation of the anterior surface of the LC. Second, biologically significant levels of strain are produced within the LC as the pressure goes from physiologic to elevated, even without considering the magnifying effects of the lamina's microarchitecture. Third, average laminar strains depend more on scleral compliance than on laminal compliance. Fourth, the simplified central retinal vasculature has surpris-

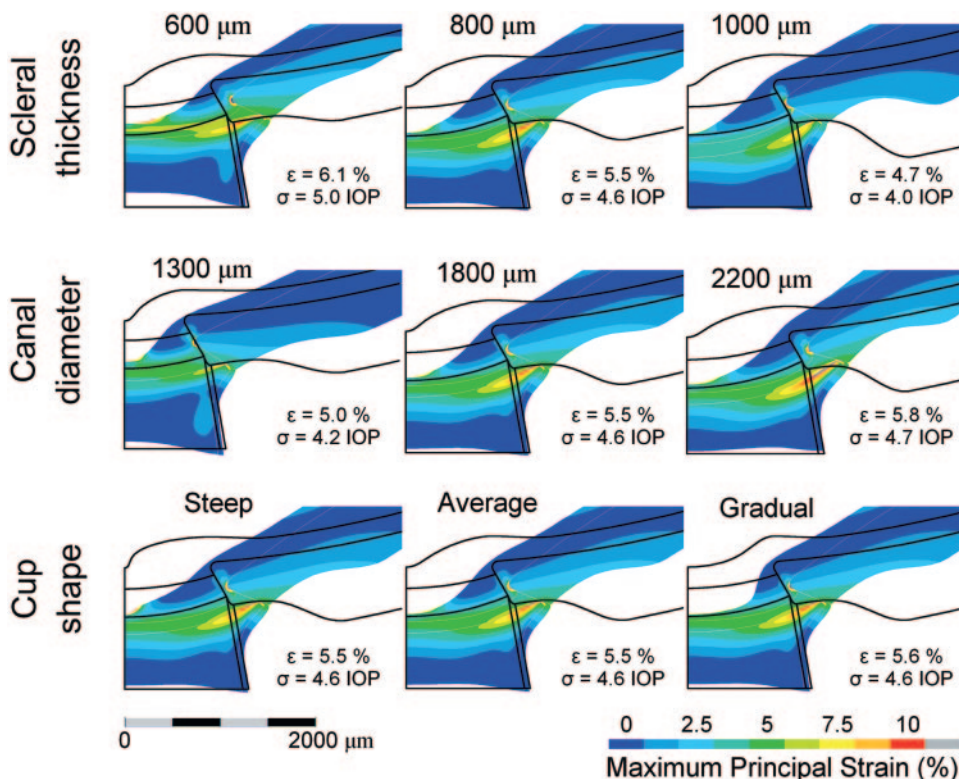


FIGURE 6. Geometric sensitivity analysis. Contour plots of computed distributions of maximum principal strain at an IOP of 50 mm Hg as a function of changes in geometry. Superimposed on each model are the edges of the undeformed configuration (0 mm Hg IOP). Geometries are variations of model 3. Colors are shown on deformations exaggerated six times. Below each computed result are the average maximum principal strain (ε) and von Mises equivalent stress (σ) within the LC. As in the other figures, deformations have been zeroed on the vitreoretinal interface at 5° from the axis of symmetry (see text for details of zeroing). Contour levels and colors are identical in all models. The largest effects occurred with variations in scleral thickness; however, cup shape had almost no effect.

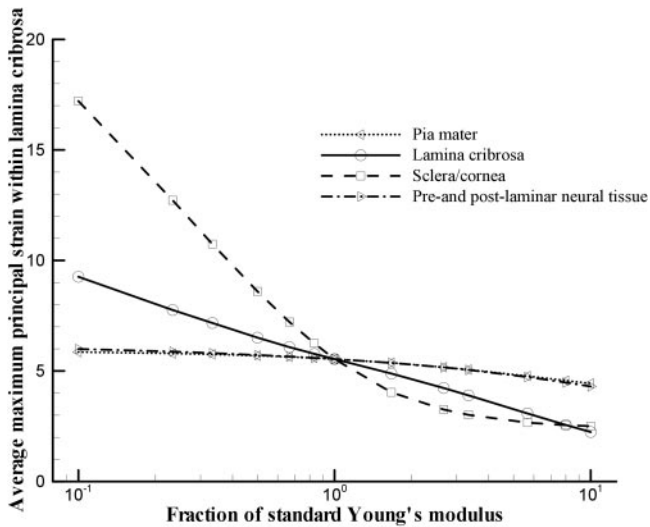


FIGURE 7. Effects of material properties on LC strain. Average maximum principal strain within the LC at an IOP of 50 mm Hg, as a function of Young's modulus. The modulus of each tissue region was varied independently and is plotted in the abscissa as a fraction of the standard Young's modulus—that is, the modulus used to compute all other figures in this work. Standard Young's moduli are: sclera/cornea and pia mater, 3 MPa; LC, 0.3 MPa; and pre- and postlaminar neural tissue, 0.03 MPa. Note the log scale of the horizontal axis. Surprisingly, changes in scleral stiffness had a larger effect on average LC maximum principal strain than those in the stiffness of the LC itself.

ingly little effect on ONH biomechanics. Let us consider each of these in turn.

Lamina Deformation Need Not Match Vitreoretinal Deformation. Pressure is a normal stress—that is, a force that, by definition, acts at 90° to any surface to which it is exposed. Therefore, when the cup walls are steep, IOP on the vitreoretinal interface induces lateral displacement, in addition to posterior displacement. This lateral displacement stretches tissue away from the center of the cup, resulting in cup enlargement, as well as deepening. This complex pattern of displacement leads to a situation in which the magnitude of optic cup deepening is not maximum at the center of the cup floor, but is offset from the center. This deformation profile was also observed experimentally, at least in some eyes (Figs. 3, 4).

The anterior surface of the lamina did not experience the same magnitude of lateral displacement forces and did not necessarily move in the same way as the vitreoretinal interface. This means that measurements of acute ONH topographic change (e.g., using the HRT) can be a poor surrogate for the displacement of the LC. The magnitude of this discrepancy is expected to be largest in cups with steep walls.

The LC Is Exposed to Biologically Significant Levels of Strain. The mechanisms by which stress and strain affect cellular functions, leading to changes in astrocyte phenotype and glaucomatous optic neuropathy, are not well understood. The disruption of axonal transport observed in glaucoma could be a consequence of cytoskeletal alterations and microtubule loss that result from transient stretch injury,⁵¹ but other cellular functions have also been shown to be affected by stress and strain, including cell adhesion, transmembrane transport, and RNA processing.^{52,53} To elucidate the possible relevance of a given level of stress or strain requires the determination of normal physiologic levels. Downs et al.²⁸ considered a physiologic level of strain in the sclera to be between 0% and 1% and suggested that levels above 3.5% could be pathophysiologic, because they result in detectable changes in scleral material properties (stiffening). Slightly higher strain levels (5%–6%) were sufficient to induce a wide range of biological effects in

neuronal cells in *in vitro* models.^{6,54} The same threshold for axonal injury was observed by Margulies and Thibault.⁵⁵ Using adult guinea pig optic nerves Bain and Meaney⁵⁶ estimated a Lagrangian strain threshold of 21% for morphologic axonal injury and 18% for deterioration of nerve function. These values are lower than the 27.1% measured in infant guinea pigs.⁵⁷ Using a mixture of experiments and computational models of a guinea pig brain Anderson⁵⁸ developed a probabilistic model of injury based on the peak von Mises stress in a region. Stresses of 27 to 43 kPa (202–322 mm Hg) resulted in 50% chance of injury in up to 20% of the affected region. Variable shear stress, such as may occur in tissue during diurnal variations in IOP, leads to injury in three times more cells than does steady shear stress.⁵⁹

The peak levels of strain and stress predicted by our models exceed most of the thresholds just quoted. Some of the extreme strains and stresses predicted by the models are due to nonphysiologic geometric details (e.g., nonrounded “corners”); however, strain levels in the LC in particular are nontrivial, consistent with the hypothesis that mechanical effects can contribute to damage to nerve fibers and loss of visual function observed in glaucoma.

Average Lamellar Strain Is Most Affected by Scleral Compliance, Less Affected by Lamellar Compliance, and Least Affected by Neural and Pia Mater Compliance. The natural variability and inherent inaccuracy in measurements of the mechanical properties of the tissues of the ONH compel us to test the effect that our choice of material properties has on our calculations. Through the parametric studies, we found that average lamellar maximum principal strain depends more on scleral than lamellar compliance, with a relatively weak dependence on neural and pia mater compliances. Further, the thickness of the sclera and the size of the scleral canal have an appreciable influence on LC strains. This suggests that for proper understanding and modeling of ONH biomechanics, it is essential to know the mechanical properties and geometry of the sclera, at least as accurately as those of the LC.

A Simplified Central Retinal Vasculature Seems to Have Little Effect on ONH Biomechanics. Except for some local stress concentrations, ONH biomechanics were only weakly affected by the simplified central retinal vasculature. This result is counter to our original expectations. Direct measurements of the mechanical properties (e.g., stiffness) of the central vessel walls and incorporation of the central retinal vasculature in a fully three-dimensional model is necessary to confirm this result. In particular, because the central retinal vascular tree branches into the prelaminar neural region, it is still possible that it plays an important role in the support of the nerve fiber layer, especially in the slowly progressing disease where tissue remodeling is important.

Limitations

The results in this study were obtained from simplified models, and naturally there are aspects of the biomechanics of the ONH that are impossible to capture. For example, with axial symmetry, it is impossible to consider any geometry other than a perfectly circular scleral canal or the oblique insertion of the optic nerve into the sclera, which could affect strain and stress levels.^{19,20} We developed the models in an attempt to identify the fundamental elements involved in ONH biomechanics, and they cannot, by definition, tell us about individual-specific aspects. They are therefore, by construction, preliminary. Still, they provide the opportunity to perform analysis in a controlled situation that incorporates potentially interesting biomechanical features. For example, they allow us to model the IOP-induced deformation of the vitreoretinal interface. Also, whereas previous models assumed that the peripheral LC is pulled by lateral forces coplanar to the undeformed LC, our

models allow for effects of peripapillary scleral thickness variations, resulting in rotation of the scleral canal in the anterior-posterior direction, akin to a twisting of the LC periphery.

Despite the idealized nature of the models, this work represents, to our knowledge, the first attempt to model in detail the depth of the human ONH from vitreoretinal interface to optic nerve. Ongoing work seeks to incorporate more physiologically accurate geometries (including detailed blood vessels), complex material properties (including anisotropy, non-linearity, and large deformation effects), and a full evaluation of the effect of CSF pressure. Use of more advanced material properties will also depend on the availability of experimental data that provide the necessary parameters and allow validation of the results.

It is important to interpret the results presented in this work in their proper context. First, we modeled the LC as a homogenous tissue, where in reality it is composed of relatively rigid connective tissue and more compliant neural tissue. The stresses and strains we computed represent averages over tissue regions larger than several LC pores; however, individual components can experience stresses or strains much larger than the average (Downs J, et al. *IOVS* 2004;45:ARVO E-Abstract 2157). This work helps establish a lower bound for the stresses and strains experienced by individual cells in the LC, as well as guiding boundary condition selection for more sophisticated models of individual laminar pores. Second, the assumed incompressibility of the tissues could also be inaccurate—for example, if elevated IOP induced axoplasmic flow from the prelaminar neural region into the LC or the postlaminar neural region.

Despite these restrictions, it is encouraging that the pattern of computed topographic change is similar to that measured experimentally, at least in some eyes (Figs. 3, 4), with maximal deflection of prelaminar neural tissues occurring in a ring at the bottom of the optic cup. Nevertheless, there is significant inter-eye variability that cannot be fully captured by generic simplified models, and the process of validation discussed herein should not be considered definitive. We intend to show only that the predicted deformations fall within the range of experimental measurements on real eyes. In addition, the use of postmortem tissue may induce artifacts, including the development of edema that could affect ONH deformation under elevated IOP. Future work will explore the development of individual-specific models, with geometries based on histologic samples and a comprehensive sensitivity analysis on geometry.

Notwithstanding the difference in scale, there is a surprising similarity in the shape of the deformation curves, shown in Figure 4, of computed IOP-induced deformations and differences between average normal and average glaucomatous eyes. Even the bend approximately 0.8 mm from the cup center is repeated. Still, our models represent only acute (passive) deformation of the tissue in response to a step change in IOP. This ignores long-term remodeling processes that distinguish glaucomatous from normal eyes, and this similarity could be a coincidence.

In closing, a consistent morphologic finding was that the sclera thins as it approaches the scleral canal, as shown in model 3. Because the sclera is the stiffest ONH tissue, it supports much of the overall load. In particular, the peripapillary sclera must support relatively high stresses, which are compounded by peripapillary scleral thinning. Our calculations suggest that peripapillary scleral thinning confers a biomechanical disadvantage, because it produces higher strains in the LC. Downs et al.⁶⁰ have identified a zone of thickened sclera surrounding the peripapillary sclera in the monkey eye. This ring would partially “shield” the scleral canal from large deformation. Evidence of such a thickened zone in the human eyes is equivocal¹² and should be further investigated.

Studies have shown that a thinner central cornea is a significant risk factor for development⁶¹ and progression⁶² of glaucomatous visual field loss. It is not yet clear whether this finding is explainable solely by artifactually low IOP readings through thin corneas, or whether there are other factors that are responsible.^{63,64} If there were a correlation between corneal thickness and scleral thickness, thinner corneas would be associated with more LC deformation at a given IOP level. This speculation remains to be tested experimentally.

In summary, despite the relative simplicity of the models presented herein, important conclusions can be made that are likely to hold true for most eyes. The deformation of the vitreoretinal interface does not necessarily correspond to that of the anterior surface of the LC; biologically significant levels of strain are produced within the LC; and average strains within the LC depend more strongly on scleral and laminar compliance than on neural and pia mater compliance.

Acknowledgments

The authors thank the Eye Bank of Canada for providing donor tissue.

References

1. Geijssen HC. *Studies on Normal Pressure Glaucoma*. Amsterdam; Kugler Publications; 1991.
2. Quigley HA, Flower RW, Addicks EM, McLeod DS. The mechanism of optic nerve damage in experimental acute intraocular pressure elevation. *Invest Ophthalmol Vis Sci*. 1980;19:505-517.
3. Yan DB, Flanagan JG, Farra T, Trope GE, Ethier CR. Study of regional deformation of the optic nerve head using scanning laser tomography. *Curr Eye Res*. 1998;17:903-916.
4. Levy NS, Crapps EE. Displacement of optic nerve head in response to short-term intraocular pressure elevation in human eyes. *Arch Ophthalmol*. 1984;102:782-786.
5. Dongqi H, Zeqin R. A biomathematical model for pressure-dependent lamina cribrosa behavior. *J Biomech*. 1999;32:579-584.
6. Edwards ME, Good TA. Use of a mathematical model to estimate stress and strain during elevated pressure induced lamina cribrosa deformation. *Curr Eye Res*. 2001;23:215-225.
7. Bauer S, Voronkova E. Mechanical aspects of the development of the glaucomatous atrophy of the optic nerve fibres. Presented at the Ocular Biomechanics Conference, Moscow. Helmholtz Research Institute for Eye Diseases; 2001.
8. Bellezza AJ, Hart RT, Burgoyne CF. The optic nerve head as a biomechanical structure: initial finite element modeling. *Invest Ophthalmol Vis Sci*. 2000;41:2991-3000.
9. Heys JJ, Barocas VH, Taravella MJ. Modeling passive mechanical interaction between aqueous humor and iris. *J Biomech Eng*. 2001;123:540-547.
10. Shin TJ, Vito RP, Johnson LW, McCarey BE. The distribution of strain in the human cornea. *J Biomech*. 1997;30:497-503.
11. Vito RP, Carnell PH. Finite element based mechanical models of the cornea for pressure and indenter loading. *Refract Corneal Surg*. 1992;8:146-151.
12. Olsen TW, Aaberg SY, Geroski DH, Edelhauser HF. Human sclera: thickness and surface area. *Am J Ophthalmol*. 1998;125:237-241.
13. Jonas JB, Mardin CY, Schlotzer-Schrehardt U, Naumann GO. Morphometry of the human lamina cribrosa surface. *Invest Ophthalmol Vis Sci*. 1991;32:401-405.
14. Jonas JB, Budde WM, Nemeth J, Grundler AE, Mistlberger A, Hayler JK. Central retinal vessel trunk exit and location of glaucomatous parapapillary atrophy in glaucoma. *Ophthalmology*. 2001;108:1059-1064.
15. Bellezza AJ, Rintalan CJ, Thompson HW, Downs JC, Hart RT, Burgoyne CF. Deformation of the lamina cribrosa and anterior scleral canal wall in early experimental glaucoma. *Invest Ophthalmol Vis Sci*. 2003;44:623-637.
16. Quigley HA, Addicks EM. Regional differences in the structure of the lamina cribrosa and their relation to glaucomatous optic nerve damage. *Arch Ophthalmol*. 1981;99:137-143.

17. Jonas JB, Budde WM. Diagnosis and pathogenesis of glaucomatous optic neuropathy: morphological aspects. *Prog Retin Eye Res.* 2000;19:1-40.
18. Jonas JB, Berenshtein E, Holbach L. Anatomic relationship between lamina cribrosa, intraocular space, and cerebrospinal fluid space. *Invest Ophthalmol Vis Sci.* 2003;44:5189-5195.
19. Jonas JB, Gusek GC, Guggenmoos-Holzmann I, Naumann GO. Size of the optic nerve scleral canal and comparison with intravitral determination of optic disc dimensions. *Graefes Arch Clin Exp Ophthalmol.* 1988;226:213-215.
20. Quigley HA, Brown AE, Morrison JD, Drance SM. The size and shape of the optic disc in normal human eyes. *Arch Ophthalmol.* 1990;108:51-57.
21. Grunwald JE, Sinclair SH, Riva CE. Is the pulsating vascular tree entoptic phenomenon an indicator of ophthalmic artery pressure? *Invest Ophthalmol Vis Sci.* 1981;20:564-566.
22. Bill A. Vascular physiology of the optic nerve. In: Varma R, Spaeth G, Parker K, eds. *The Optic Nerve in Glaucoma.* Philadelphia: Lippincott Williams & Wilkins; 1992:37-50.
23. Phillips JR, McBrien NA. Form deprivation myopia: elastic properties of sclera. *Ophthalmic Physiol Opt.* 1995;15:357-362.
24. Siegwart JT Jr, Norton TT. Regulation of the mechanical properties of tree shrew sclera by the visual environment. *Vision Res.* 1999;39:387-407.
25. Smolek M. Elasticity of the bovine sclera measured with real-time holographic interferometry. *Am J Optom Physiol Opt.* 1988;65:653-660.
26. Woo SL, Kobayashi AS, Schlegel WA, Lawrence C. Nonlinear material properties of intact cornea and sclera. *Exp Eye Res.* 1972;14:29-39.
27. Friberg TR, Lacey JW. A comparison of the elastic properties of human choroid and sclera. *Exp Eye Res.* 1988;47:429-436.
28. Downs JC, Suh JK, Thomas KA, Bellezza AJ, Burgoyne CF, Hart RT. Viscoelastic characterization of peripapillary sclera: material properties by quadrant in rabbit and monkey eyes. *J Biomech Eng.* 2003;125:124-131.
29. Battaglioli JL, Kamm RD. Measurements of the compressive properties of scleral tissue. *Invest Ophthalmol Vis Sci.* 1984;25:59-65.
30. Kobayashi AS, Woo SL, Lawrence C, Schlegel WA. Analysis of the corneo-scleral shell by the method of direct stiffness. *J Biomech.* 1971;4:323-330.
31. Miller K. Constitutive model of brain tissue suitable for finite element analysis of surgical procedures. *J Biomech.* 1999;32:531-537.
32. Guillaume A, Osmont D, Gaffie D, Sarron JC, Quandieu P. Effects of perfusion on the mechanical behavior of the brain-exposed to hypergravity. *J Biomech.* 1997;30:383-389.
33. Metz H, McElhaney J, Ommaya AK. A comparison of the elasticity of live, dead, and fixed brain tissue. *J Biomech.* 1970;3:453-458.
34. Jones IL, Warner M, Stevens JD. Mathematical modelling of the elastic properties of retina: a determination of Young's modulus. *Eye.* 1992;6:556-559.
35. Chang GL, Hung TK, Feng WW. An in-vivo measurement and analysis of viscoelastic properties of the spinal cord of cats. *J Biomech Eng.* 1988;110:115-122.
36. Ozawa H, Matsumoto T, Ohashi T, Sato M, Kokubun S. Comparison of spinal cord gray matter and white matter softness: measurement by pipette aspiration method. *J Neurosurg.* 2001;95:221-224.
37. Bellezza AJ. *Biomechanical Properties of the Normal and Early Glaucomatous Optic Nerve Head: an Experimental and Computational Study Using the Monkey Model.* New Orleans, LA: Department of Biomedical Engineering, Tulane University; 2002. Doctoral thesis.
38. Zhivoderov NN, Zavalishin NN, Neniukov AK. Mechanical properties of the dura mater of the human brain [in Russian]. *Sud Med Ekspert.* 1983;26:36-37.
39. Mazuchowski EL, Thibault LE. Biomechanical properties of the human spinal cord and pia mater. Presented at the Summer Bioengineering Conference, Key Biscayne, FL; ASME June, 2003.
40. Brands DWA. *Predicting Brain Mechanics During Closed Head Impact: Numerical And Constitutive Aspects.* Eindhoven, The Netherlands: Technische Universiteit; 2002. Doctoral thesis.
41. Kleiven S. *Finite Element Modeling of the Human Head.* Stockholm, Sweden: Department of Aeronautics, Royal Institute of Technology; 2002. Doctoral thesis.
42. ANSYS. ANSYS v 6.1 Online Reference Manual, Theory Reference, Section 19.7. Swanson Analysis Systems Inc. Canonsburg, PA: Ansys Inc. (www.ansys.com).
43. Woo SL, Kobayashi AS, Lawrence C, Schlegel WA. Mathematical model of the corneo-scleral shell as applied to intraocular pressure-volume relations and applanation tonometry. *Ann Biomed Eng.* 1972;1:87-98.
44. Ethier CR, Tertinegg I, Yan DB, Trope GE, Flanagan JG. A system for studying lamina cribrosa biomechanics in human eyes. In Blanchard SM, ed. Presented at the First Joint Meeting of Biomedical Engineering Society (BMES) and Engineering in Medicine and Biology Society (EMBS). Atlanta: IEEE; 1999:1312-1313.
45. Rohrschneider K, Burk RO, Volcker HE. Reproducibility of topometric data acquisition in normal and glaucomatous optic nerve heads with the laser tomographic scanner. *Graefes Arch Clin Exp Ophthalmol.* 1993;231:457-464.
46. Silver DM, Geyer O. Pressure-volume relation for the living human eye. *Curr Eye Res.* 2000;20:115-120.
47. Swindale NV, Stjepanovic G, Chin A, Mikelberg FS. Automated analysis of normal and glaucomatous optic nerve head topography images. *Invest Ophthalmol Vis Sci.* 2000;41:1730-1742.
48. Timoshenko S, Goodier J. *Theory of Elasticity.* New York: McGraw-Hill; 1970.
49. Heickell AG, Bellezza AJ, Thompson HW, Burgoyne CF. Optic disc surface compliance testing using confocal scanning laser tomography in the normal monkey eye. *J Glaucoma.* 2001;10:369-382.
50. Wang L, Damji KF, Munger R, et al. Increased disk size in glaucomatous eyes vs normal eyes in the Reykjavik eye study. *Am J Ophthalmol.* 2003;135:226-228.
51. Jafari SS, Maxwell WL, Neilson M, Graham DI. Axonal cytoskeletal changes after non-disruptive axonal injury. *J Neurocytol.* 1997;26:207-221.
52. Ellis EF, McKinney JS, Willoughby KA, Liang S, Povlishock JT. A new model for rapid stretch-induced injury of cells in culture: characterization of the model using astrocytes. *J Neurotrauma.* 1995;12:325-339.
53. Hernandez MR. The optic nerve head in glaucoma: role of astrocytes in tissue remodeling. *Prog Retin Eye Res.* 2000;19:297-321.
54. Triyoso DH, Good TA. Pulsatile shear stress leads to DNA fragmentation in human SH-SY5Y neuroblastoma cell line. *J Physiol.* 1999;515:355-365.
55. Margulies SS, Thibault LE. A proposed tolerance criterion for diffuse axonal injury in man. *J Biomech.* 1992;25:917-923.
56. Bain AC, Meaney DF. Tissue-level thresholds for axonal damage in an experimental model of central nervous system white matter injury. *J Biomech Eng.* 2000;122:615-622.
57. Prange MT, Margulies SS. Tissue strain thresholds for axonal injury in the infant brain. Presented at the ASME 2001 Bioengineering Conference, Snowbird, UT, June 27-July 1, 2001:833-834.
58. Anderson RWG. *A Study on the Biomechanics of Axonal Injury.* Adelaide, Australia: Road Accident Research Unit and the Department of Mechanical Engineering, The University of Adelaide; 2000. Doctoral thesis.
59. Lamb RG, Harper CC, McKinney JS, Rzigalinski BA, Ellis EF. Alterations in phosphatidylcholine metabolism of stretch-injured cultured rat astrocytes. *J Neurochem.* 1997;68:1904-1910.
60. Downs JC, Blidner RA, Bellezza AJ, Thompson HW, Hart RT, Burgoyne CF. Peripapillary scleral thickness in perfusion-fixed normal monkey eyes. *Invest Ophthalmol Vis Sci.* 2002;43:2229-2235.
61. Brandt JD, Beiser JA, Kass MA, Gordon MO. Central corneal thickness in the Ocular Hypertension Treatment Study (OHTS). *Ophthalmology.* 2001;108:1779-1788.
62. Medeiros FA, Sample PA, Zangwill LM, Bowd C, Aihara M, Weinreb RN. Corneal thickness as a risk factor for visual field loss in patients with preperimetric glaucomatous optic neuropathy. *Am J Ophthalmol.* 2003;136:805-813.
63. Cioffi GA, Liebmann JM. Translating the OHTS results into clinical practice. *J Glaucoma.* 2002;11:375-377.
64. Girkin C, Cioffi GA, Liebmann J. Thin corneas and the risk of progression (Letter). *J Glaucoma.* 2003;12:445-446; author reply 446.